Journal of Zhejiang University-SCIENCE A 2025 26(10):983-996
www.jzus.zju.edu.cn; www.springer.com/journal/11582
E-mail: jzus_a@zju.edu.cn

Research Article
https://doi.org/10.1631/jzus.A2400555

Check for updates

Effect of side track height on aerodynamic characteristics of a high-speed high-temperature superconducting maglev train under crosswind

Yiming PAN[1], Zongpeng LI[1], Xiaofei WANG[1], Hongmin ZHAO[2], Weihua ZHANG[2,3], Zigang DENG[2,3]✉

[1]*School of Mechanics and Aerospace Engineering, Southwest Jiaotong University, Chengdu 610031, China*
[2]*State Key Laboratory of Rail Transit Vehicle System, Southwest Jiaotong University, Chengdu 610031, China*
[3]*Research Center for Super-High-Speed Evacuated Tube Maglev Transport, Southwest Jiaotong University, Chengdu 610031, China*

Abstract: Currently, the design of high-temperature superconducting (HTS) maglev trains adopts a U-shaped track operation mode, and the height of the side track significantly impacts the train's aerodynamic characteristics. In this study, we used computational fluid dynamics (CFD) methods, based on the 3D Reynolds-averaged Navier-Stokes (RANS) method and shear stress transport (SST) k-ω turbulence model, to deeply investigate the effects of the presence or absence of a U-shaped track and different side track heights (800, 880, and 960 mm) on the pressure distribution, velocity distribution, and flow field structure of HTS maglev trains at a speed of 400 km/h under crosswinds. The numerical methods were verified using a scaled ICE-2 model wind tunnel test. First, the aerodynamic characteristics of the train under different wind direction angles with and without side tracks were studied. We found that the aerodynamic performance of the train is the most adverse when the wind direction angle is 90°. The presence of a U-shaped track can effectively reduce the lateral force, lift, and yawing moment of the train. The aerodynamic performance of the first suspension bogie at the bottom, which is the worst, will also be effectively improved. Next, the aerodynamic effects of different side track heights on the HTS maglev train were studied. An increase in side track height will reduce the lift and lateral force of the train, while the increase in drag is relatively small. Under the premise of ensuring passengers can conveniently alight, we found that a U-shaped track with a side track height of 960 mm has the best aerodynamic performance. The research findings offer a valuable reference for the engineering application and design of the track structure of HTS maglev train systems.

Key words: High-temperature superconducting (HTS); High-speed maglev train; U-shaped track; Crosswind; Numerical simulation

1 Introduction

High-speed maglev transportation is a pivotal focus for the future advancement of rail transit on a global scale. Some high-speed maglev trains have adopted U-shaped tracks, and one of their most significant features is their side tracks. For instance, the track of China's Fenghuang Maglev Sightseeing Express is laid on U-shaped beams (Peng et al., 2023). The U-shaped track side walls of superconducting electrodynamic suspension (EDS) trains are arranged in a continuous fashion with propulsion coils and coils for 8-shaped levitation and guidance (Huang H et al., 2024). In January 2021, the world's first high-temperature superconducting (HTS) pinning high-speed maglev engineering prototype train and test line, designed and developed in China, were officially put into use at Southwest Jiaotong University and used a U-shaped track (Wang et al., 2021). The HTS maglev is one type of high-speed maglev technology. Due to its significant advantages in energy saving, environmental friendliness, low noise, comfort, and high-speed operation potential, it is currently being actively designed for engineering applications (Deng et al., 2021, 2022). The HTS maglev train runs at a high speed, but it is also prone to lateral disturbances, especially under the influence

✉ Zigang DENG, deng@swjtu.cn
Yiming PAN, https://orcid.org/0009-0003-8598-0430
Zongpeng LI, https://orcid.org/0000-0002-3162-6992
Xiaofei WANG, https://orcid.org/0000-0003-1489-196X
Zigang DENG, https://orcid.org/0000-0001-7937-9081

Received Dec. 3, 2024; Revision accepted Apr. 7, 2025;
Crosschecked Sept. 18, 2025

of crosswinds. Therefore, it is necessary to focus on studying how to reduce the impact of crosswinds.

Numerous scholars have undertaken extensive research into the operation of trains in crosswind conditions. They have conducted investigations into the behavior of high-speed trains under the influence of strong crosswinds using wind tunnel experiments, actual vehicle tests, and numerical simulations (Suzuki et al., 2001; Dorigatti et al., 2015; Tian, 2019; Neto et al., 2021; Wang et al., 2022; Yang et al., 2022; Zhang et al., 2024). Baker et al. (2004) conducted research into the measurement methodology for aerodynamic forces and stability within a crosswind scenario, integrating wind tunnel scale models with actual vehicle tests to develop a comprehensive analytical framework. Meng et al. (2020) explored the effect of the levitation gap on the lift performance of maglev trains in crosswind scenarios, using a blend of numerical simulation methodologies and wind tunnel experiments. Nowadays, the main research method focuses on numerical simulation. Zhang and Ishihara (2024) used numerical simulation techniques to evaluate the lateral wind stability of railway vehicles. Gao et al. (2025) investigated the aerodynamic properties of trains subjected to crosswinds, using three distinct track models for their study. Luo et al. (2023) investigated the transient aerodynamic behavior and flow patterns surrounding high-speed trains as they enter tunnels in the presence of crosswinds. High-speed maglev trains are subjected to significant aerodynamic forces during operation under crosswinds. As a result, researchers have undertaken numerous aerodynamic studies on maglev trains in the presence of crosswinds. Li ZP et al. (2023) investigated the effects of aerodynamic loads under crosswind conditions on passenger comfort and safety. Huang ZD et al. (2024) investigated the aerodynamic properties of high-speed maglev trains with variable formation lengths in the presence of crosswinds. Zhu et al. (2024) investigated the transient aerodynamic behavior of high-speed maglev trains undergoing plate braking at various crosswind velocities (Zhu et al., 2024).

At present, the methods used to mitigate the risks associated with crosswinds on train operations center mainly on barriers and blowing control. Li XZ et al. (2023) conducted a study on the aerodynamic characteristics of a fully enclosed sound barrier during the passage of a train. Yan et al. (2025) discovered that wind barriers are effective in diminishing the aerodynamic forces acting on road vehicles when exposed to high wind yaw angles. Liang et al. (2024) introduced a novel windscreen design, which integrates fence-type and perforated wind barriers, enhancing the aerodynamic performance of a train-bridge system. Zhao et al. (2024) found that a windbreak with a 30% ventilation rate provides the best performance, ensuring the highest level of safety and stability for train operations. Niu et al. (2018) discovered that windbreak walls can improve the aerodynamic properties of trains when exposed to crosswind conditions. Guo et al. (2024) found that blowing air can reduce the lateral force exerted on the head car by up to 15%, effectively lowering the risk of maglev trains operating in crosswind conditions. Xu et al. (2024) revealed that the lateral force on a train is substantially diminished when the angle between the eddy current generator and the relative wind is set to 30°.

A U-shaped track, as a unique structural feature of the HTS maglev train system, exerts a greater aerodynamic influence on the underside of the train. The track mitigates the impact of crosswinds on the underside of the train and so can reduce the negative impact of crosswinds to some extent. However, there is almost no research on the aerodynamics of U-shaped tracks, so conducting relevant research is essential. The side track height of a U-shaped track is an important parameter that requires extensive research. Changing the side track height will significantly impact the distribution of pressure across the train's surface and the surrounding flow field structure. It will also affect the aerodynamic performance of the suspension bogies, thereby affecting levitation and guidance performance. Therefore, in this paper, we describe the aerodynamics of the unique U-shaped track and focus on analyzing its effect under crosswinds.

We established a high-precision model of an HTS pinning high-speed maglev engineering prototype vehicle and a U-shaped track. Based on the 3D Reynolds-averaged Navier-Stokes (RANS) method and shear stress transport (SST) k-ω turbulence model (where k is the turbulent kinetic energy and ω is the specific dissipation rate), we investigated the impact of the U-shaped track's presence or absence, as well as various side track heights, on the pressure distribution, velocity distribution, and flow field structure of a maglev train, to enhance its safety and efficiency during operation.

The subsequent sections of this paper are organized as follows: Section 2 provides a detailed exposition of the study's model and then introduces numerical models, including the computational fluid dynamics (CFD) computational domain, the grids and numerical methods used, mesh independence analysis, and the CFD simulation validation. Section 3 showcases and discusses the outcomes of the CFD simulations. Ultimately, the main conclusions drawn from the investigation are highlighted in Section 4.

2 Numerical method

2.1 Geometry model

Fig. 1 depicts a full-scale model of an HTS maglev train, including a train simulation model and a physical model. The head of the simulation model references the prototype of the HTS maglev head car (Fig. 1c). The model has undergone detailed modeling, featuring windshields and suspension bogies, which show the devices that provide levitation and guidance forces for the HTS maglev train—namely, the superconducting levitators. Additionally, the base of the train model clearly shows the U-shaped track, linear motor, and the unique permanent magnet guideway (PMG) specific to the HTS maglev train.

The height of the train is H (H=3.35 m), with a total length of about 18.31H (61.35 m), and a width of about 0.866H (2.90 m). The train is composed of three carriages: a head car, a middle car, and a tail car. There are two windshields: windshield 1 (W1) situated between the head car and the middle car, and windshield 2 (W2) between the middle car and the tail car. Each carriage has three suspension bogies at the bottom, totaling nine suspension bogies. These bogies are numbered consecutively from the head car to the tail car as B1–B9.

2.2 Computational domain and boundary conditions

The U-shaped track model is shown in Fig. 2. The track system consists of a high-thrust linear motor stator, the PMG, which provides an external magnetic field, and the side track. The absence of a side track can be considered as a track with a height of 225 mm, which can also be regarded as a non-existent side track, later denoted as NT (no side track). According to the actual model, the side track height of the actual U-shaped track is 880 mm, which is subsequently represented by WT-880 (with track). The impact of the side track height on train aerodynamics was studied. When investigating the variation in the side track height, it is essential to consider the amplitude of this variation. We defined this amplitude as the distance from the permanent magnet eddy current brake (Zhang GW et al., 2022) on the side track to the uppermost part of the U-shaped track in the test line. This definition ensures that potential issues related to the installation of the permanent magnet eddy current brake can be avoided in subsequent practical applications. This distance is set at 80 mm, the minimum value for the side track height is 800 mm, and the maximum value is

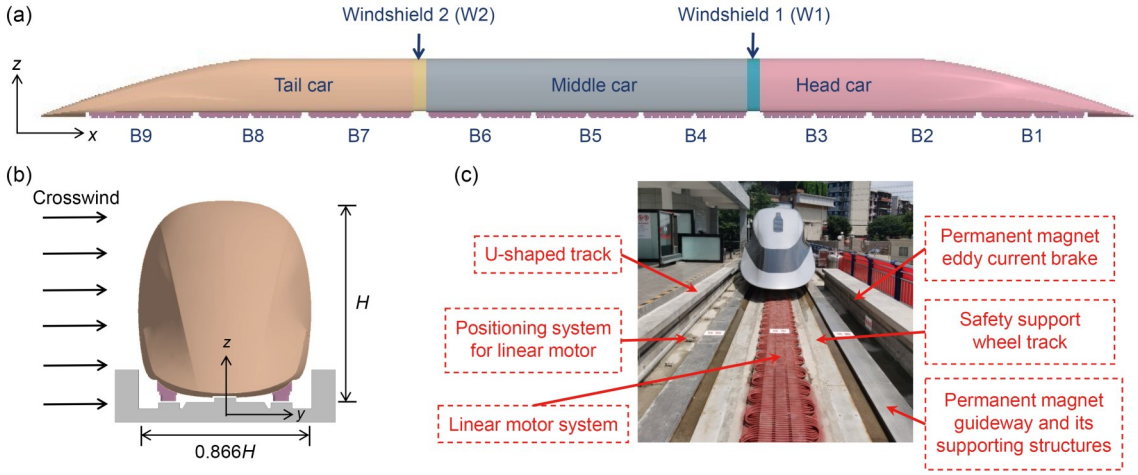

Fig. 1 HTS maglev train model, vehicle prototype, test line, and U-shaped track: (a) side view of the HTS maglev train model; (b) front view of the HTS maglev train model; (c) HTS magnetic levitation engineering prototype head car and U-shaped track

960 mm. The two scenarios are denoted as WT-800 and WT-960, respectively. Additionally, the increase and decrease in height also guarantee the convenience of passenger boarding and alighting.

Since the most expensive part of the HTS high-speed maglev train line lies in the PMG, and because the cement material required for changes in the height of the U-shaped side track is relatively inexpensive, with the volume of the height-variable section of the U-shaped track being one-fortieth of the base volume, the cost of cement used for the height changes of the side track in actual construction does not need to be considered.

In this study, based on the wake characteristics of trains under crosswind conditions and the literature (Zhang et al., 2013), we established a computational domain with dimensions as shown in Figs. 3a and 3b. The computational domain measures 119.4H (400 m) in length, 23.88H (80 m) in height, and 90.66H (303.7 m) in width. Along the x-axis, the leading edge of the maglev train is 29.85H (100 m) from the inlet of the computational domain, and its trailing edge is 71.25H (238.7 m) from the outlet. Along the y-axis, the train is located 29.85H (100 m) from the inlet of the computational domain and 59.7H (200 m) from the outlet. A stationary train model was used to simulate the aerodynamic behavior of the train under a crosswind condition. The boundary conditions include a free-flow environment surrounding the computational domain (Wang et al., 2022). The ground and track are designed as no-slip moving walls, while the top surface has a symmetric boundary. Within this computational domain, the train remains stationary, while the track and ground move in the $-x$ direction at 400 km/h. The inlet flow velocity U_R represents the vector sum of the train speed U_x (−400 m/s) and the crosswind speed U_W (20 m/s).

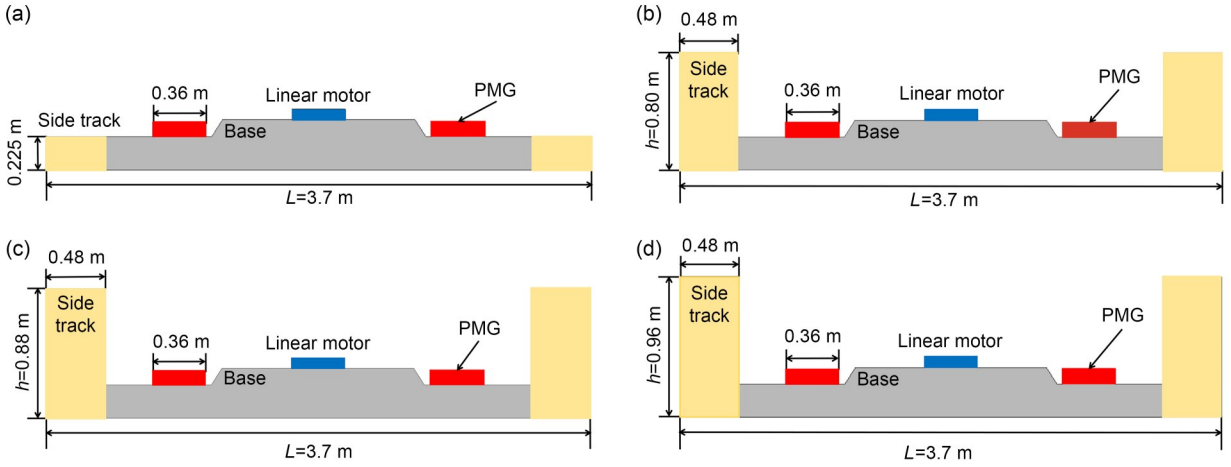

Fig. 2 Track models under different calculation conditions: (a) NT; (b) WT-800; (c) WT-880; (d) WT-960. *h* is the side track height; *L* is the bottom track width

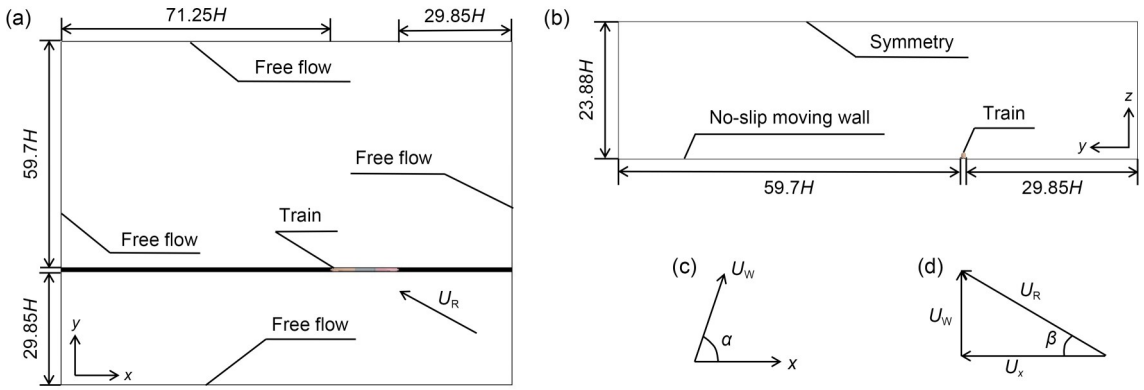

Fig. 3 Computational domain and boundary conditions of the numerical simulation: (a) top view of the computational domain; (b) front view of computational domain; (c) wind direction angle; (d) yaw angle

As shown in Figs. 3c and 3d, the wind direction angle α is defined as the angle between the crosswind and the x-axis, and the train yaw angle β is defined as the angle between the direction of the resultant wind (U_R) and the train's speed (U_x).

2.3 Mesh generation

We used STAR-CCM+ software to construct the computational mesh, and a trimmed cell mesh generator to divide the external flow field area of the maglev train, creating a prism layer mesh near the surface of the train to precisely capture the flow characteristics in the vicinity of the wall. The prism layer consists of 23 layers, using a growth factor of 1.2. The first-layer mesh thickness was set to 0.011 mm, reaching a total thickness of 3.26 mm. Referencing Chen et al. (2019), we densified the mesh around the maglev train (Fig. 4). Four refinement blocks are strategically positioned around the maglev train, with sizes of 0.04 m, 0.16 m, 0.32 m, and 0.64 m, respectively, in sequence. A refinement block with a size of 0.02 m is also added between the head car and linear motor, the tail car and linear motor, as well as between the suspension bogies and the track. The total cell count amounts to 32.7 million.

2.4 Numerical method and data processing

In this study, we observed that as the train's speed reaches 400 km/h, the compressibility of air becomes a factor that must be considered (Baker, 2014; Zhou et al., 2022). Our model is based on the SST k-ω turbulence model using the RANS method for steady-state calculations. The SST k-ω model can solve the sensitivity issue of free inflow port boundary conditions (Niu et al., 2020; Hu et al., 2021, 2022; Zhang J et al., 2022; Wang et al., 2023). Yang (2023) suggested using steady-state numerical simulation methods when studying the effects of parameters such as train speed, wind speed, and number of carriages on the magnitude of aerodynamic force. Therefore, we adopted a steady-state approach for calculations.

The definitions of the non-dimensional aerodynamic force coefficient and pressure coefficient are as follows:

$$q_\infty=\frac{1}{2}\rho U^2, \tag{1}$$

$$C_i=\frac{F_i}{q_\infty S}, \tag{2}$$

$$C_p=\frac{P-P_\infty}{q_\infty}, \tag{3}$$

where q_∞ is the dynamic pressure; ρ is the air density, 1.225 kg/m^3; U is the resultant velocity; C_i is the force coefficient; F_i is the aerodynamic force in the x-, y-, or z-direction; S is the orthographic area of the maglev train or the suspension bogies, with sizes of 8.45 m^2 and 0.444 m^2, respectively; C_p is the pressure coefficient; P and P_∞ are the surface static pressure of the train and the reference pressure in the far-field (101325 Pa), respectively.

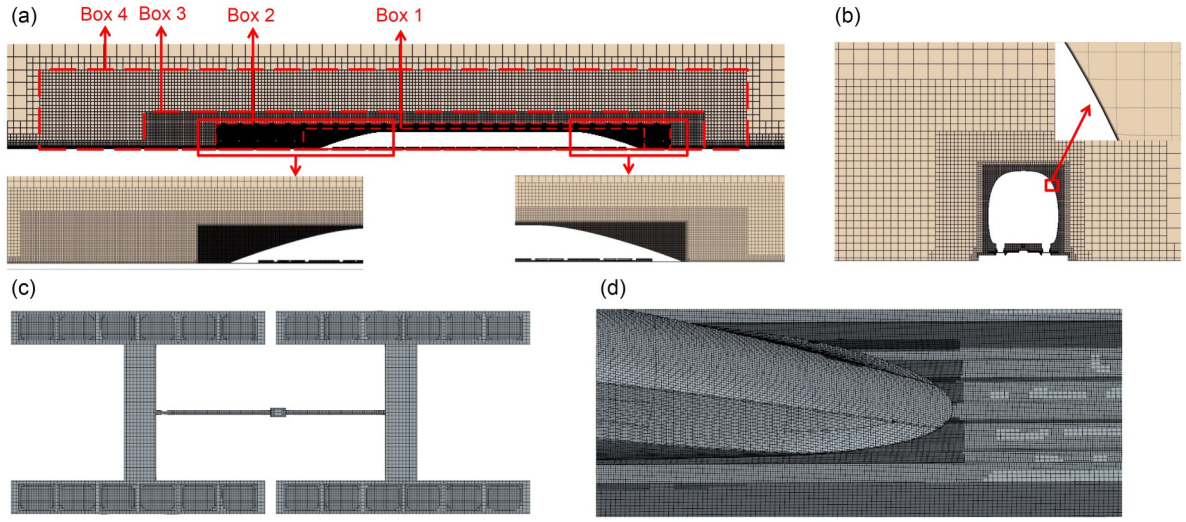

Fig. 4 Mesh display chart: (a) side view of the mesh around the train; (b) front view of the mesh and boundary layers; (c) mesh of the suspension bogie; (d) mesh of the track and head car

2.5 Grid independence validation and numerical method validation

Table 1 shows the drag coefficient C_d of the maglev train at three different mesh densities: coarse, medium, and fine. The error of the coarse mesh compared to the fine mesh is four times larger than that of the medium mesh compared to the fine mesh. Fig. 5 shows the top pressure distribution in areas such as the rear of the middle car, W2, and the front of the tail car. Fig. 5 shows that the pressure distribution of the medium mesh closely resembles that of the fine mesh, while the pressure distribution of the coarse mesh differs significantly from that of the fine mesh, mainly at the windshield and the connection between the windshield and the tail car. Additionally, there is a small fluctuation in pressure in the middle car body. These results indicate that when the number of meshes exceeds 32.7 million, the mesh density has a smaller impact on computational accuracy. Considering the computational cost, the medium mesh was chosen for the train calculations. Fig. 6 shows the y^+ distribution of the train's upper surface center line. Most of the values of y^+ in the figure are less than 1, which meets the requirement of the SST k-ω turbulence model for the mesh.

At present, there are no wind tunnel or full-scale experimental data available for the HTS maglev train. We selected the German ICE-2 train, which is a 1:10 scale model, and conducted simulation calculations under a crosswind condition using the wind tunnel experimental parameters for the ICE-2 train model (Table 2), comparing the computational outcomes with the experimental data from the wind tunnel. Figs. 7a and 7b show the 1:10 scale model of the ICE-2 train, including the front and rear of the train. The dimensions of this model are roughly consistent with the wind tunnel test model detailed by Hemida and Krajnović (2009). The height H_T of the train model is about 0.41 m, the width is about $0.74H_T$ (0.302 m), and the total length is about $8.73H_T$ (3.58 m). The ICE-2 computational domain is basically the same as the external flow field of the HTS maglev train model in this study. The boundary conditions are also the same as those for the numerical calculation of the HTS maglev train.

The planes at $3.75H_T$ (1.54 m) and $4.88H_T$ (2 m) from the frontmost point of the car were extracted, and the body surface pressure coefficients obtained from numerical simulation and wind tunnel testing were compared on these planes (Figs. 7f and 7g). Although the results match, there are slight differences between the numerical simulation and wind tunnel test results. This is because the ICE-2 train model used in the wind tunnel test has bogies and dampers, but these are replaced by a cylinder in the model used in the simulation. Nevertheless, the discrepancies observed between the simulation and experimental results fall within an acceptable range, suggesting that the numerical simulation approach used in this study is valid.

Table 1 Train drag coefficients at different mesh densities

Mesh type	Number of mesh cells	Drag coefficient, C_d	Error compared to fine mesh
Coarse mesh	22.7 million	0.318	5.30%
Medium mesh	32.7 million	0.306	1.30%
Fine mesh	44.2 million	0.302	–

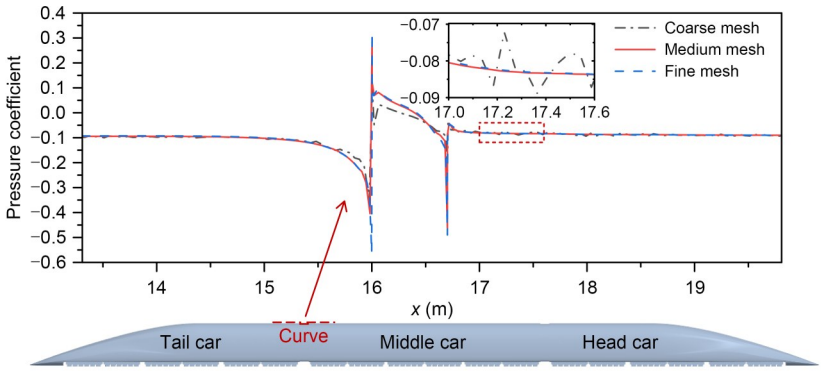

Fig. 5 Pressure distribution on the upper surface of the rear of the middle car, W2, and the front of the tail car

3 Results and discussion

3.1 Aerodynamic loads of the train with or without the side track

Firstly, we conducted an in-depth study on the drag coefficient, lateral force coefficient, and lift coefficient of each part of the train at different wind direction angles (Fig. 8). As the wind direction angle increases from 0° to 180°, it is clear that all the curves of the force coefficients for the head car, middle car, and tail car exhibit symmetry along the wind direction angle of 90°. Therefore, we describe only the influence under the wind direction angle of 0°–90°. In addition, the presence of the U-shaped track significantly influences the performance of each train car body. Compared with the NT condition, under the WT-880 condition, the drag of the head car consistently increases, while

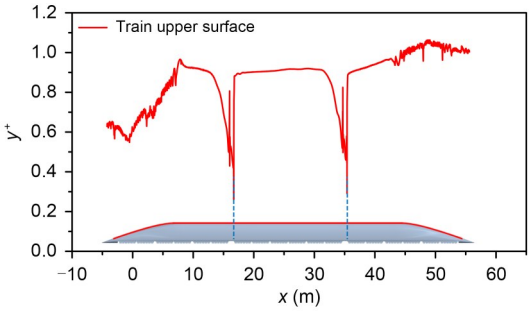

Fig. 6 y^+ distribution on the train's upper surface center line

Table 2 Wind tunnel experimental parameters for the ICE-2 train model

Experimental parameter	Value
Resultant wind velocity (m/s)	70
Yaw angle (°)	30
Turbulence intensity (%)	0.5
Reynolds number	1.4×10^{-6}
Scale size	1:10

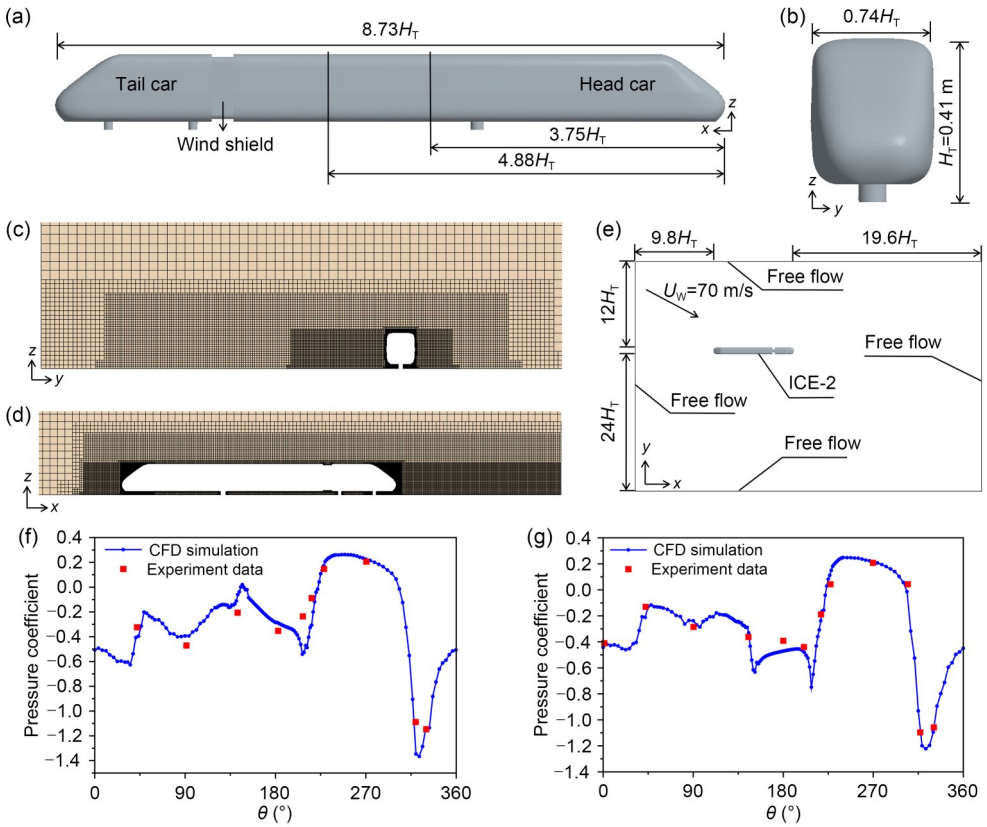

Fig. 7 Model, mesh, computational domain, simulation results, and test results of the ICE-2 train: (a) side view of the ICE-2 train model; (b) front view of the ICE-2 train model; (c) front view of the ICE-2 train model mesh; (d) side view of ICE-2 train model mesh; (e) top view of the computational domain; (f) train surface pressure coefficient on the intercepted plane of x=3.75H_T; (g) train surface pressure coefficient on the intercepted plane of x=4.88H_T. θ is the angle between the line connecting the monitoring point to the center of the section and the +z direction

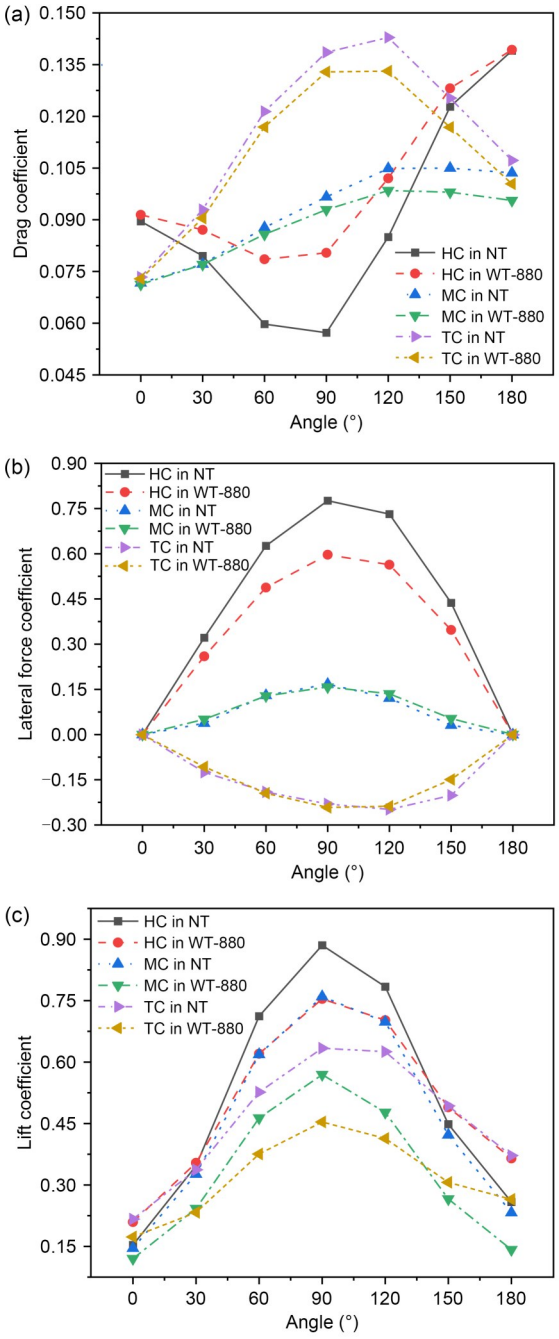

Fig. 8 Drag coefficient (a), lateral force coefficient (b), and lift coefficient (c) of the head car, middle car, and tail car at different wind direction angles. HC, MC, and TC represent the head car, middle car, and tail car, respectively

the drag of the middle and tail cars always decreases. At the same time, the lateral force of the head car decreases, whereas the changes in the lateral force of the middle and tail cars are relatively small. When the wind direction angle approaches 90°, the lift of the head car diminishes, whereas it rises when the angle is 0°. The lift of the middle and tail cars continuously decreases. Although the drag of the head car increases near 90° and the lift of the head car increases near 0°, these forces are smaller than those at other angles. This phenomenon demonstrates that the presence of the U-shaped track can effectively minimize the negative influence of crosswind on the head, middle, and tail cars of the train.

When the wind direction angle approaches 90°, the lateral force and lift force experienced by the head, middle, and tail cars all reach their peak values and the drag force on the tail car also reaches its maximum. This suggests that the train's aerodynamic efficiency is notably compromised when the wind approaches at a 90° angle. Therefore, it is essential to perform a thorough analysis of the crosswind at a 90° wind direction angle. Fig. 9 shows a detailed analysis of the forces and moments on the entire train under two conditions, NT and WT-880. Compared to the condition NT, the existence of the U-shaped track results in a slight increase in train resistance, but a substantial decrease

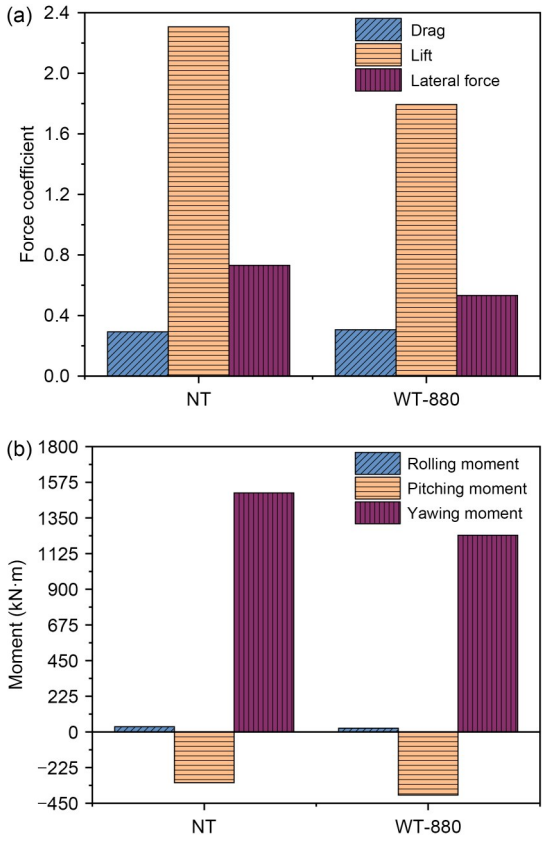

Fig. 9 Force coefficient and moment of the train under the NT and WT-880 conditions: (a) force coefficient; (b) moment

in lift and lateral force. It also leads to a decrease in the rolling and yawing moment, although the pitching moment increases. Notably, the yawing moment experienced by the train remains the largest even after the reduction. This phenomenon confirms that the presence of the U-shaped track significantly enhances the stability of the train.

Fig. 10 illustrates the pressure curves of the train at section z=0.6157 m, showing the pressure characteristics on the windward and leeward sides of the train along this section. The height of this section is consistent with the top of the side track in the WT-880 condition. From Fig. 10, under two conditions, the overall trend of the pressure curve is similar. Whether on the windward or leeward side, the pressure fluctuations on the head and tail cars at this section are significantly stronger than those on the middle car. Further observation reveals that the pressure peaks are concentrated in the windshield area, and the pressure changes there are extreme. Specifically, on the leeward side without the side track, the pressure coefficients at the ends of the two windshields reach the lowest values (−0.468 for W1 and −0.536 for W2), while on the windward side without the side track, the pressure coefficient at the end of W1 is the highest (0.370), and on the leeward side without the side track W2 shows the highest pressure coefficient (0.319). This suggests that the U-shaped track plays a role in mitigating the pressure fluctuations of the train's windshield. In the head car section, the windward side pressure consistently remains higher than on the leeward side. When x>45 m (the junction between the streamlined and non-streamlined parts of the head car), the pressure on the leeward side with the side track is generally higher than without the track, but within the x<45 m range, the situation is reversed. For the head car under the WT-880 condition, the windward side pressure is always below that of the NT condition. This shows that the presence of the U-shaped track can significantly reduce the pressure difference along this section in the x>45 m area. As for the middle car, the pressure on the windward side is invariably higher than that on the leeward side, and the fluctuations in pressure on the leeward side are more pronounced. In the tail car area, when x>7 m (the junction between the streamlined and non-streamlined parts of the tail car), the windward side pressure is greater than that on the leeward side, while when x< 7 m, the pressure on the leeward side is higher. Especially at x=−2.5 m, there is a significant pressure fluctuation. The pressure fluctuation on the windward side without the track is extreme, with the minimum pressure coefficient approaching −0.336. This phenomenon is attributable mainly to the presence of the streamlined protrusion at the tail of the train. This indicates that the U-shaped track plays a positive role in reducing the pressure fluctuations at this location. In summary, the windshields and the streamlined design parts of the head and tail cars are the areas where the train surface pressure fluctuations are the most severe, and these regions exert a substantial influence on the pressure exerted upon the train's surface.

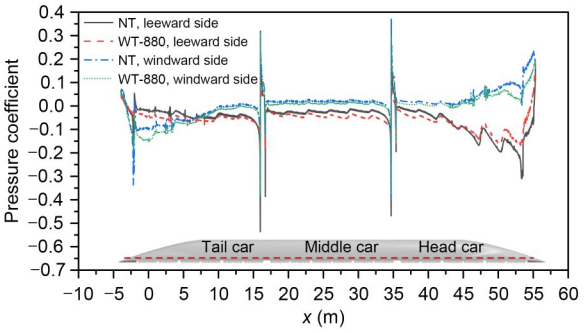

Fig. 10 Pressure coefficient curves along z=0.6157 m section of the train under the NT and WT-880 conditions

We set up two test lines, Line 1 and Line 2, respectively, as shown in Figs. 11a and 11b. Line 1 is on the leeward side and Line 2 is on the windward side above the side track, both standing at a height of 2 m above the ground. The pressure fluctuation trends on Line 1 and Line 2 show a high degree of similarity under the NT and WT-880 conditions. Taking W1 as the dividing point, compared to the NT condition, the presence of the side track causes an increase in pressure before the windshield, but after W2, the U-shaped track allows for a reduction in pressure. Looking at Line 2, the presence or absence of the U-shaped track affects mainly the pressure at the part before W1, and the presence of the U-shaped track effectively reduces the pressure in this area. This observation indicates that the U-shaped track has a more significant impact on the pressure fluctuation on the leeward side than the windward side, while the impact on the windward side is focused mainly on the head car part.

Furthermore, we studied the straight Line 3 at the bottom of the train (Fig. 11c), which is located in the narrow gap between the train and the track. The pressure reaches its maximum at the bottom of the

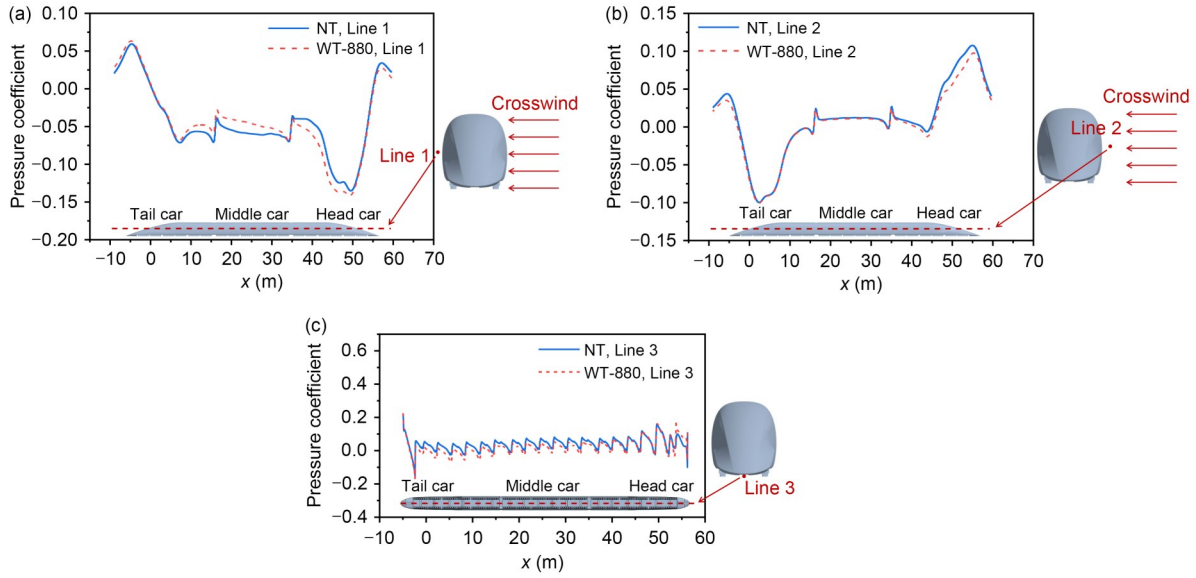

Fig. 11 Pressure coefficient distribution of leeward side, windward side, and bottom lines of the train under the NT and WT-880 conditions: (a) Line 1; (b) Line 2; (c) Line 3

head car and the tail car, and the pressure at the front position is particularly prominent. This is due to the violent fluctuation that occurs when the airflow enters the narrow space between the bottom of the train and the motor. Concurrently, the bottom of the train exhibits a regular fluctuation pattern. As the airflow flows through the area between the suspension frame beams, the pressure gradually rises. When the airflow crosses the beam area, the pressure gradually falls. In the area after B1, when under the WT-880 condition, the pressure on the line is always lower than that under the NT condition. In the area of B1, the pressure fluctuation under the WT-880 condition is more severe than that under the NT condition, indicating that the U-shaped track exerts a significant influence on the pressure fluctuation within this region.

3.2 Pressure distribution and flow field of the train

Fig. 12 shows pressure cloud diagrams of the surface of the train. At the head car on the leeward side, the pressure on the streamlined surface under the WT-880 condition is significantly higher than that under the NT condition. However, the pressure variation on the windward side of the train is not substantial. Additionally, under the influence of crosswind, the front of the train is subjected to greater pressure, and the pressure distribution under the NT condition will be more biased towards the windward side than under the WT-880 condition. We selected a plane at a height of z=0.32 m to analyze the flow field distribution characteristics at the bottom of the train (Fig. 13). Specifically, Figs. 13a and 13b show the pressure distribution nephograms under the NT and WT-880 conditions on the plane. The significant pressure fluctuation areas are concentrated at the bottom of the B1 bogie. On the leeward side of the bogies, there are three regions of low pressure, located at the head, the middle of the B1 bogie, and the head of the B2 bogie. The presence of the U-shaped track significantly reduces the area of the low-pressure zones, especially at the middle of B1 and the head of B2. Next, we conducted a detailed analysis of the flow field at the bottom of the B1 bogie.

According to results in Fig. S1 of the electronic supplementary materials (ESM), the flow field velocity at the bottom of the suspension bogie is comparatively sluggish. The R2 area at the head of the B1 bogie is the most turbulent. In the R1 area on the windward side, the flow field is chaotic, while the flow in the R4 area on the leeward side is relatively stable. The R2 area under the WT-880 condition shows higher symmetry than the NT condition, which is attributable mainly to the mitigating influence of the track on the crosswind effect. At the same time, the number of vortices in the R2 area under the WT-880 condition increases, while a vortex appears in the R3 area under the NT condition but not under the WT-880 condition.

We extracted five sections parallel to the y-z plane for flow field analysis, as shown in Fig. S2 of the ESM.

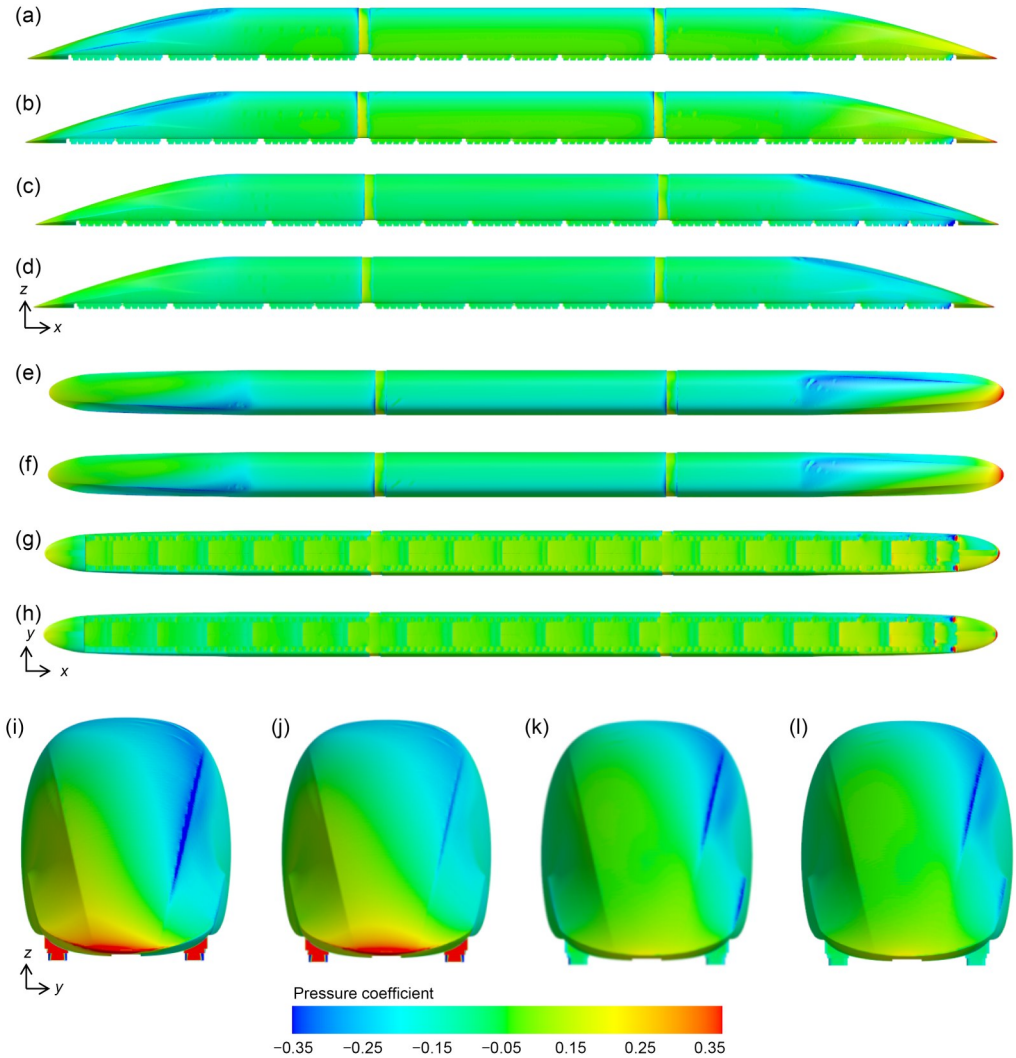

Fig. 12 Train surface pressure cloud diagrams under the NT and WT-880 conditions: (a) windward side pressure (NT); (b) windward side pressure (WT-880); (c) leeward side pressure (NT); (d) leeward side pressure (WT-880); (e) upper surface pressure (NT); (f) upper surface pressure (WT-880); (g) lower surface pressure (NT); (h) lower surface pressure (WT-880); (i) front surface pressure (NT); (j) front surface pressure (WT-880); (k) back surface pressure (NT); (l) back surface pressure (WT-880)

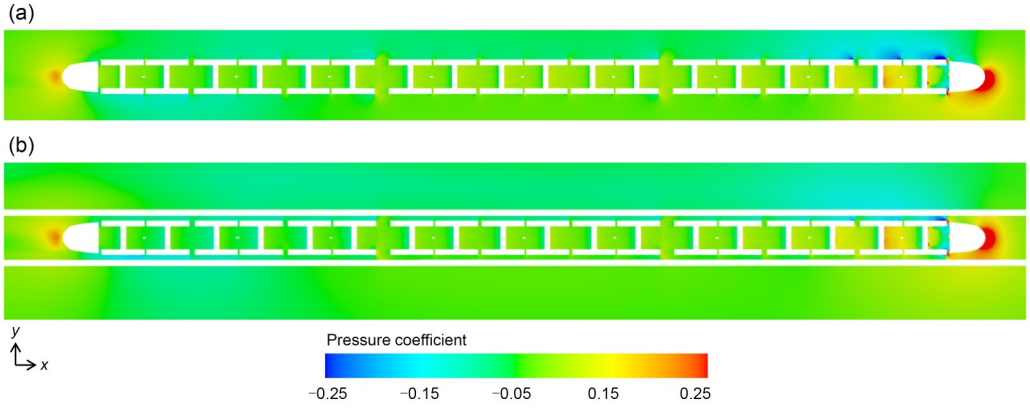

Fig. 13 Pressure coefficient distribution in the plane at a height of z=0.32 m under different conditions: (a) NT; (b) WT-880

The *x*-coordinates of these five sections are 0.35 m, 8 m, 26.1 m, 43 m, and 51 m, corresponding to the streamlined part of the tail car, the junction of the streamlined and non-streamlined parts of the tail car, the middle section of the middle car, the junction of the streamlined and non-streamlined parts of the head car, and the streamlined part of the head car, respectively. From the head car to the tail car, these five sections are designated I, II, III, IV, and V.

Under the NT condition, section I presents two significant vortex structures (V1 and V2 in Fig. S2). V1 is located on the left side of the base, close to the ground, while V2 is located on the right side below the front of the car, suspended above the base, not in contact with the ground. The flow velocity of V1 is significantly faster than that of V2. From section I to section II, V1 gradually expands, while V2 gradually diminishes. In section III, a new small vortex V4 has been generated on the right upper side, with a very small velocity, and V2 has completely dissipated. When the section moves to V, V1 begins to shift to the left upper side. For the WT-880 condition, section I also forms two vortices, V1 and V3, but V1 is larger because of the side track's influence. At the same time, the intervention of the side track promotes the emergence of V3 and causes V2 to disappear. As the section moves from I to III, V3 gradually disappears, V1 and three new vortices, V4, V5, and V6, are generated. V5 is formed by the interaction between the train and the upper edge of the side track. V6 is located on the right upper side of the bottom of the train, which indicates that the flow under the train is more complex than under the NT condition. When the section reaches IV, V5 gradually expands. When it reaches V, V5 has completely disappeared, due to the reduction in the train's sectional area. Overall, whether or not the U-shaped track is present, the air needs to pass through the narrow gap between the superconducting levitator and the track, which leads to the bottom area exhibiting turbulent characteristics, with very slow flow velocity. For the WT-880 condition, the narrow gap formed by the side track and the car body causes the flow velocity to decrease, further intensifying the complexity of the airflow. However, at the junction of the streamlined and non-streamlined sections of the head car, the airflow velocity near the inner wall of the side track experiences a significant increase due to the expansion of the gap.

We studied the effect of the presence or absence of a U-shaped track on the aerodynamic characteristics of the suspension bogies and the impact of side track height on the aerodynamic characteristics. Due to space constraints, this section of content, along with the corresponding figures and table, has been placed in the ESM.

4 Conclusions

In this study, we investigated the aerodynamic performance of an HTS maglev train under crosswind with four different track models, namely with a track height of 225 mm (no side track), 800 mm, 880 mm, and 960 mm. The study focused mainly on the pressure distribution on the train surface, the surrounding velocity distribution, and the flow field structure. The following conclusions were reached:

(1) When the wind angle is from 0° to 180°, the drag, lateral force, and lift of the head, middle, and tail cars of the HTS maglev train generally exhibit symmetry along the wind direction angle of 90°. When the wind direction angle approaches 90°, the lateral force and lift on each car and the drag on the tail car reach their maximum values. Under a 90° wind direction angle, the aerodynamic performance of the train is relatively poor. The presence of the U-shaped track can effectively reduce the drag of the middle and tail cars and the lateral force of the head car.

(2) When the wind direction angle is 90°, the presence of the U-shaped track significantly reduces the lateral force, lift, and yawing moment of the train. It promotes the symmetry of the airflow in the B1 bogie area at the bottom of the train, although the pressure fluctuations in this area are somewhat intensified. The aerodynamic performance of the B1 bogie is the least effective, but the presence of the U-shaped track significantly improves this situation. The U-shaped track has many positive effects on the train, so its installation is strongly recommended.

(3) As the side track height is gradually increased from 800 mm to 960 mm, the lateral force and lift of the train are significantly reduced. This also effectively reduces the drag, lateral force, rolling moment, pitching moment, and yawing moment of the suspension bogie. Therefore, in practical applications, we recommend the use of a side track with a height of 960 mm

in the four working conditions studied to optimize the aerodynamic performance of the train.

Acknowledgments

This work is supported by the National Natural Science Foundation of China (No. U23A20681) and the S&T Program of Hebei Province, China (No. 23567602H).

Author contributions

Yiming PAN conducted the numerical calculation and wrote the first draft of the manuscript. Zongpeng LI, Xiaofei WANG, Hongmin ZHAO, and Zigang DENG revised the final version. Weihua ZHANG and Zigang DENG provided computing resources.

Conflict of interest

Yiming PAN, Zongpeng LI, Xiaofei WANG, Hongmin ZHAO, Weihua ZHANG, and Zigang DENG declare that they have no conflict of interest.

References

Baker CJ, 2014. A review of train aerodynamics. Part 1–fundamentals. *The Aeronautical Journal*, 118(1201):201-228. https://doi.org/10.1017/S000192400000909X

Baker CJ, Jones J, Lopez-Calleja F, et al., 2004. Measurements of the cross wind forces on trains. *Journal of Wind Engineering and Industrial Aerodynamics*, 92(7-8):547-563. https://doi.org/10.1016/j.jweia.2004.03.002

Chen ZW, Liu TH, Yan CG, et al., 2019. Numerical simulation and comparison of the slipstreams of trains with different nose lengths under crosswind. *Journal of Wind Engineering and Industrial Aerodynamics*, 190:256-272. https://doi.org/10.1016/j.jweia.2019.05.005

Deng ZG, Wang L, Li HT, et al., 2021. Dynamic studies of the HTS maglev transit system. *IEEE Transactions on Applied Superconductivity*, 31(5):3600805. https://doi.org/10.1109/tasc.2021.3052452

Deng ZG, Zhang WH, Wang L, et al., 2022. A high-speed running test platform for high-temperature superconducting maglev. *IEEE Transactions on Applied Superconductivity*, 32(4):3600905. https://doi.org/10.1109/tasc.2022.3143474

Dorigatti F, Sterling M, Baker CJ, et al., 2015. Crosswind effects on the stability of a model passenger train—a comparison of static and moving experiments. *Journal of Wind Engineering and Industrial Aerodynamics*, 138:36-51. https://doi.org/10.1016/j.jweia.2014.11.009

Gao HR, Liu TH, Gu HY, et al., 2025. Effects of rail models on aerodynamic characteristics of trains in crosswinds at a large yaw angle. *Mechanics Based Design of Structures and Machines*, 53(3):2093-2115. https://doi.org/10.1080/15397734.2024.2402391

Guo ZJ, Guo ZH, Chen ZW, et al., 2024. On the active flow control in maglev train safety under crosswinds: analysis of leeward suction and blowing action. *Physics of Fluids*, 36(9):095130. https://doi.org/10.1063/5.0224211

Hemida H, Krajnović S, 2009. Exploring flow structures around a simplified ICE2 train subjected to a 30° side wind using LES. *Engineering Applications of Computational Fluid Mechanics*, 3(1):28-41. https://doi.org/10.1080/19942060.2009.11015252

Hu X, Deng ZG, Zhang WH, 2021. Effect of cross passage on aerodynamic characteristics of super-high-speed evacuated tube transportation. *Journal of Wind Engineering and Industrial Aerodynamics*, 211:104562. https://doi.org/10.1016/j.jweia.2021.104562

Hu X, Deng ZG, Zhang JW, et al., 2022. Aerodynamic behaviors in supersonic evacuated tube transportation with different train nose lengths. *International Journal of Heat and Mass Transfer*, 183:122130. https://doi.org/10.1016/j.ijheatmasstransfer.2021.122130

Huang H, Li HT, Coombs T, et al., 2024. Advancements in dynamic characteristics analysis of superconducting electrodynamic suspension systems: modeling, experiment, and optimization. *Superconductivity*, 11:100114. https://doi.org/10.1016/j.supcon.2024.100114

Huang ZD, Zhou ZB, Chang N, et al., 2024. Aerodynamic features of high-speed maglev trains with different marshaling lengths running on a viaduct under crosswinds. *Computer Modeling in Engineering & Sciences*, 140(1):975-996. https://doi.org/10.32604/cmes.2024.047664

Li XZ, Qiu XW, Zheng J, et al., 2023. Aerodynamic characteristics of fully enclosed sound barrier induced by the passing trains with 400 km/h. *Journal of Wind Engineering and Industrial Aerodynamics*, 241:105518. https://doi.org/10.1016/j.jweia.2023.105518

Li ZP, Wang XF, Ding Y, et al., 2023. Study on the dynamics characteristics of HTS maglev train considering the aerodynamic loads under crosswinds. *Sustainability*, 15(23):16511. https://doi.org/10.3390/su152316511

Liang HB, Zou YF, Zhang YL, et al., 2024. Effects of combined-type wind barriers on the aerodynamic characteristics of train–bridge system for a long-span suspension bridge. *Physics of Fluids*, 36(8):083608. https://doi.org/10.1063/5.0221243

Luo JJ, Wang L, Shang SY, et al., 2023. Study of unsteady aerodynamic performance of a high-speed train entering a double-track tunnel under crosswind conditions. *Journal of Fluids and Structures*, 118:103836. https://doi.org/10.1016/j.jfluidstructs.2023.103836

Meng S, Zhou D, Meng S, 2020. Effect of rail gap on aerodynamic performance of maglev train. *Journal of Central South University (Science and Technology)*, 51(12):3537-3545 (in Chinese). https://doi.org/10.11817/j.issn.1672-7207.2020.12.027

Neto J, Montenegro PA, Vale C, et al., 2021. Evaluation of the train running safety under crosswinds–a numerical study on the influence of the wind speed and orientation considering the normative Chinese Hat Model. *International Journal of Rail Transportation*, 9(3):204-231.

https://doi.org/10.1080/23248378.2020.1780965

Niu JQ, Zhou D, Liang XF, 2018. Numerical investigation of the aerodynamic characteristics of high-speed trains of different lengths under crosswind with or without windbreaks. *Engineering Applications of Computational Fluid Mechanics*, 12(1):195-215. https://doi.org/10.1080/19942060.2017.1390786

Niu JQ, Wang YM, Liu F, 2020. Numerical study on the effect of damaged windows on aerodynamic characteristics of passenger trains under strong crosswind. *Proceedings of the Institution of Mechanical Engineers, Part C: Journal of Mechanical Engineering Science*, 234(15):2994-3003. https://doi.org/10.1177/0954406220911396

Peng YY, Zhao CF, Wang SD, et al., 2023. Mechanical behaviors of the U-girder for urban maglev transit under temperature loads and train loads. *Journal of Vibration and Control*, 30(21-22):4888-4902. https://doi.org/10.1177/10775463231214822

Suzuki M, Tanemoto K, Maeda T, 2001. Aerodynamic characteristics of train/vehicles under cross winds. *Journal of Wind Engineering*, 89:505-508.

Tian HQ, 2019. Review of research on high-speed railway aerodynamics in China. *Transportation Safety and Environment*, 1(1):1-21. https://doi.org/10.1093/tse/tdz014

Wang F, Guo ZH, Shi ZL, et al., 2023. A study of crosswind characteristics on aerodynamic performance of high-speed trains on embankment. *Iranian Journal of Science and Technology, Transactions of Mechanical Engineering*, 47(2):417-431. https://doi.org/10.1007/s40997-022-00534-9

Wang S, Li HT, Wang L, et al., 2021. Suspension parameters optimization of HTS maglev under random vibration. *IEEE Transactions on Applied Superconductivity*, 31(8):3603704. https://doi.org/10.1109/tasc.2021.3094427

Wang XF, Hu X, Wang JK, et al., 2022. Safety analysis of high temperature superconducting maglev train considering the aerodynamic loads under crosswinds. *Proceedings of the Institution of Mechanical Engineers, Part C: Journal of Mechanical Engineering Science*, 237(10):2279-2290. https://doi.org/10.1177/09544062221140033

Xu B, Liu TH, Shi X, et al., 2024. Mitigation of crosswind effects on high-speed trains using vortex generators. *Physics of Fluids*, 36(7):075199. https://doi.org/10.1063/5.0218270

Yan L, Li JL, He XH, et al., 2025. Ride comfort assessment of road vehicles on a long-span truss girder suspension bridge under crosswinds. *Engineering Structures*, 322:119112. https://doi.org/10.1016/j.engstruct.2024.119112

Yang B, Xiong XH, He Z, et al., 2022. Feasibility of replacing the 3-coach with a 1.5-coach grouping train model in wind tunnel experiment at different yaw angles. *Journal of Central South University*, 29(6):2062-2073. https://doi.org/10.1007/s11771-022-5060-3

Yang YG, 2023. The Aerodynamic Performances of the High-Speed Maglev Train in the Open Air and the Local Optimization of the Train Head. PhD Thesis, Lanzhou Jiaotong University, Lanzhou, China (in Chinese). https://doi.org/10.27205/d.cnki.gltec.2023.000021

Zhang DQ, Ishihara T, 2024. A comparative study on the crosswind stability of the railway vehicle considering distinct national standards. *Journal of Wind Engineering and Industrial Aerodynamics*, 254:105901. https://doi.org/10.1016/j.jweia.2024.105901

Zhang GW, Zhu JM, Li Y, et al., 2022. Simulation of the braking effects of permanent magnet eddy current brake and its effects on levitation characteristics of HTS maglev vehicles. *Actuators*, 11(10):295. https://doi.org/10.3390/act11100295

Zhang J, Adamu A, Su XC, et al., 2022. Effect of simplifying bogie regions on aerodynamic performance of high-speed train. *Journal of Central South University*, 29(5):1717-1734. https://doi.org/10.1007/s11771-022-4948-2

Zhang QY, Zhou SQ, Xu G, et al., 2024. Integrated CFD and MBD methods for dynamic performance analysis of a high-speed train transitioning through varied windbreak corridor designs. *Journal of Wind Engineering and Industrial Aerodynamics*, 250:105755. https://doi.org/10.1016/j.jweia.2024.105755

Zhang WH, Shen ZY, Zeng J, 2013. Study on dynamics of coupled systems in high-speed trains. *Vehicle System Dynamics*, 51(7):966-1016. https://doi.org/10.1080/00423114.2013.798421

Zhao L, Yang WC, Liu YK, et al., 2024. Effects of windbreak types on aerodynamics of high-speed trains traversing from flat ground to semi-cutting and semi-embankment under crosswinds. *Physics of Fluids*, 36(7):075115. https://doi.org/10.1063/5.0212334

Zhou P, Qin D, Zhang JY, et al., 2022. Aerodynamic characteristics of the evacuated tube maglev train considering the suspension gap. *International Journal of Rail Transportation*, 10(2):195-215. https://doi.org/10.1080/23248378.2021.1885514

Zhu FT, Xie JW, Lv DZ, et al., 2024. Transient aerodynamic behavior of a high-speed maglev train in plate braking under crosswind. *Physics of Fluids*, 36(3):035133. https://doi.org/10.1063/5.0189686

Electronic supplementary materials

Sections S1 and S2, Figs. S1–S9, Table S1